



Bifunctional Co active site on dilute CoCu plasmonic alloy for light-driven H₂ production from methanol and water

Wen-Ning Lu^{a,b}, Shunqin Luo^{b,*}, Yibo Zhao^a, Jianbing Xu^a, Gaoliang Yang^c, Emmanuel Picheau^b, Minmin Han^{b,d}, Qi Wang^b, Sijie Li^b, Lulu Jia^b, Ming-Xing Ling^a, Tetsuya Kako^e, Jinhua Ye^{b,f,g,**}

^a State Key Laboratory of Nuclear Resources and Environment, East China University of Technology, Nanchang 330013, China

^b International Center for Materials Nanoarchitectonics (WPI-MANA), National Institute for Materials Science (NIMS), 1-1 Namiki, Tsukuba, Ibaraki 305-0044, Japan

^c Institute of Materials Research and Engineering (IMRE), Agency for Science, Technology and Research (A*STAR), 2 Fusionopolis Way, Innovis #08-03, Singapore 138634, Singapore

^d National Engineering Research Center for Intelligent Electrical Vehicle Power System, College of Mechanical and Electrical Engineering, Qingdao University, Qingdao, Shandong 266071, China

^e Hydrogen Production Catalyst Materials Group, Research Center for Energy and Environmental Materials (GREEN), National Institute for Materials Science (NIMS), 1-1 Namiki, Tsukuba, Ibaraki 305-0044, Japan

^f Graduate School of Chemical Sciences and Engineering, Hokkaido University, Sapporo, Hokkaido 060-0814, Japan

^g TJU-NIMS International Collaboration Laboratory, School of Materials Science and Engineering, Tianjin University, Tianjin 300072, China

ARTICLE INFO

Keywords:

CoCu plasmonic alloy
Solar-driven reaction
Methanol activation
Water activation
Hydrogen Production

ABSTRACT

Catalytic H₂ production from CH₃OH and H₂O is acknowledged as a promising strategy in the growth of future hydrogen economy, yet its industrialization still faces significant challenges of substantial energy consumption. To overcome the high barrier of CH₃OH/H₂O activation, we report a low-cost plasmonic Co–Cu alloy catalyst for producing H₂ efficiently through a light-driven process, bringing an outstanding generation rate of 6225.1 μmol g^{−1} min^{−1} (31.1 μmol min^{−1}) without external thermal energy input. The bifunctional nature of Co active sites on Cu favors the adsorption of CH₃OH and lowers the energy barrier for H₂O dissociation simultaneously. Moreover, the Co–Cu interface exploits the hot-carrier-induced reactant activation upon visible light irradiation, enormously decreasing the apparent activation energy from 100.8 to 68.2 kJ mol^{−1}. Our study unveils a novel method to harness renewable solar energy for H₂ production, and will provide numerous opportunities for constructing a robust and sustainable catalytic process.

1. Introduction

Given the significant energy and environmental issues associated with conventional fossil fuels, it becomes an essential task for searching a clean and renewable energy alternative, particularly in the current context of the appeal for carbon neutrality [1–3]. Hydrogen (H₂) stands out as a green energy carrier and exhibits the potential for sustainable utilization [4–7], but is somewhat limited by drawbacks of large-scale storage and transportation [8,9]. In order to resolve these shortcomings, on-demand H₂ production from a stable and bio-renewable liquid was proposed, which utilizes methanol (CH₃OH) as an ideal liquid

organic hydrogen carrier (LOHC) and releases H₂ with a high storage density in the process of reforming with H₂O vapor (methanol steam reforming, MSR) [10–12]. The state-of-the-art procedures for MSR using catalysts based on earth-abundant elements (e.g., copper-based and nickel-based materials) typically require relatively high reaction temperatures (250–350 °C) [13,14]. Recent advances have been made in low temperature region, in which the noble-metal-catalysts and/or high reaction pressure are needed to break kinetic limitations (e.g., activating C–H and O–H bond of CH₃OH and H₂O, respectively) [10,15,16]. The development of an affordable and facile catalytic process for MSR holds paramount importance, which involves the construction of advanced

* Corresponding author.

** Corresponding author at: International Center for Materials Nanoarchitectonics (WPI-MANA), National Institute for Materials Science (NIMS), 1-1 Namiki, Tsukuba, Ibaraki 305-0044, Japan.

E-mail addresses: LUO.Shunqin@nims.go.jp (S. Luo), Jinhua.YE@nims.go.jp (J. Ye).

<https://doi.org/10.1016/j.apcatb.2023.123520>

Received 28 August 2023; Received in revised form 27 October 2023; Accepted 13 November 2023

Available online 16 November 2023

0926-3373/© 2023 Elsevier B.V. All rights reserved.

non-noble-metal-based catalysts capable of using renewable stimulus.

The natural sunlight shows the prospect to mitigate the reliance on un-renewable fossil fuels [17–19]. Recent pioneering researches exemplified that the solar light can be harnessed by plasmonic metal-based materials (e.g., Au, Ag, and Cu) for driving surface catalytic reactions through the contribution of photo-induce local heating and/or energetic hot carriers [20–24]. A range of energy-demanding reactions, which were originally driven by the thermal-energy, have been explored using plasmonic photocatalysis (e.g., N₂ fixation [25,26], and CO₂ reduction [27–29]), delivering even superior performance compared to thermocatalytic counterparts [30]. In order to favor the hot carrier-induced bond activation process during plasmonic photocatalysis [31], “antenna-reactor” catalysts composing plasmonic nanocrystals (antenna) and surface deposited active sites (reactor) have been proposed recently [20]. For instance, our previous work demonstrated the construction of Cu–Zn surface alloy for solar-driven methanol steam reforming [32]. Upon light excitation, surface Zn active sites could pump the hot electrons from Cu to surface H₂O molecules, leaving electron-deficient Cu for activating CH₃OH, thereby enabling a concerted and full activation of surface reactants. Similar geometry design concept can be found in other plasmonic nanostructures, such as Cu–Ru [20], Cu–Pt [33], Al–Pd [34] and Au–Pd [35]. Whilst their impressive catalytic performance, the use of noble metals as catalytically active sites indispensably increases the capital cost, which encourages researchers to design non-noble-metal-based plasmonic nanostructures.

Co-based materials demonstrated unique capacity for adsorption and partial dissociation of carbon species, and therefore are generally considered to be active for synthesizing C₂₊ products through CO₂ hydrogenation or Fischer-Tropsch process [36–38]. Furthermore, recent research proved that atomic-dispersed Co sites could also serve as co-catalysts that are highly active for H₂O reduction [39]. These previous findings inspire us to introduce Co active site into Cu as a secondary metal, which could potentially influence the binding strength of some critical adsorbates as well as to facilitate the H₂O activation, enabling an efficient H₂ production [40,41].

In this work, a highly dilute CoCu plasmonic alloy (Co_{0.08}Cu_{99.92}) was reported, which delivered an outstanding catalytic activity for solar-driven MSR with a H₂ generation rate of 6225.1 μmol g^{−1} min^{−1} (without external thermal energy input). We found that with the concerted contribution of both photo-induced charge carriers and Co active sites, the apparent activation energy was decreased from 100.8 to 68.2 kJ mol^{−1}. In-situ investigations combined with finite difference time domain (FDTD) simulation and density functional theory (DFT) calculations revealed that the introduction of Co in Cu can promote CH₃OH adsorption and H₂O dissociation by the local polarization, and the hot carriers further stimulate the conversion of both CH₃OH and H₂O at Co–Cu interface. These findings expand the horizons of research focused on the development of cost-effective Cu-based catalyst systems, which can be utilized for the MSR and other energy-demanding reactions upon solar irradiance.

2. Experimental section

2.1. Synthesis of Cu and CoCu plasmonic catalysts

Wet chemistry method using NaBH₄ as reducing agent was employed to fabricate Cu and CoCu alloy nanoparticles (NPs). For the fabrication of Cu, firstly, a mixture was prepared by combining 20 ml of ascorbic acid (0.1 M) with 100 ml Cu(NO₃)₂•3H₂O (0.01 M) and PVP (molar ratio of Cu to PVP=50:1) solution. NaBH₄ aqueous solution (10 ml, 0.1 M), serving as reducing agent, was added into above mixture, followed by adding 500 mg of SiO₂ as inert support for NPs. The solution was stirred for 30 min and subsequently ultra-sonicated for 10 min. After reaction completed, the precipitate was separated from the solution through centrifugation, washed by ultrapure water and dried overnight at 70 °C. Then, the catalysts were calcinated in air at 350 °C for 4 h. The synthesis

method of CoCu NPs is similar to that of Cu, but with the inclusion of Co (NO₃)₂•6H₂O as the source of Co. Before activity measurement and characterization, the catalysts were subjected to a reduction process in a H₂ atmosphere at 350 °C, resulting in the formation of SiO₂-supported metallic Cu or CoCu NPs (referred to as Cu or CoCu, hereafter). For comparison, impregnation method was employed to fabricate SiO₂-supported noble-metal-based catalysts, including 1.0 wt% of Pt, Pd and Au.

2.2. Photocatalytic activity measurement

The solar-driven MSR reaction was conducted using solar energy. AM 1.5 light was utilized as illuminant, and the diameter of irradiation was 10 mm. The light intensity was adjusted by changing the input current of illuminant. The surface temperature of catalysts upon light irradiation was recorded by thermocouple. Before measurement, the materials were reduced in a H₂ atmosphere. The gaseous reactants were bubbled into reaction chamber through a CH₃OH/H₂O solution (volume ratio 1/1) with a flow rate of 50 ml min^{−1}. Gas chromatography (GC) equipped with thermal conductivity detector (TCD) and flame ionization detector (FID) were employed to quantify the products. The solar energy conversion efficiency can be evaluated as below:

$$\eta = \frac{\alpha \text{ (mol} \cdot \text{s}^{-1}) \times \Delta H_{\text{MSR}}^0 \text{ (J} \cdot \text{mol}^{-1})}{\text{light power (J s}^{-1})} \times 100\% \quad (1)$$

where α is H₂ production rate, and ΔH_{MSR}^0 is the standard reaction enthalpy changes of MSR (48.97 kJ mol^{−1}).

The photo-assisted thermocatalytic MSR was characterized by a self-made photo-assisted thermocatalytic reactor to probe the underlying mechanism of Co active sites and photo-induced hot carriers. LA-251 Xe lamp coupled with optical filters (HA30 and L42) was used to provide visible light irradiance, and the light was introduced into the reactor through a quartz window with irradiation diameter of 8.5 mm. The desired temperature of the catalyst was regulated by a resistive heater managed by a temperature controller. 5 mg catalyst was in-situ reduced in a H₂ atmosphere at 350 °C, afterwards, the Ar was injected into the reactor to remove the H₂ before reaction started. During reaction, the space velocity of gaseous reactants was 30 ml min^{−1}, and the measurement method of products was as same as in solar-driven catalysis. The apparent quantum efficiency (AQE) was calculated as: AQE (%) = [(Y_{light} − Y_{dark}) × 2] / number of incident photons × 100, where Y_{light} and Y_{dark} are the amounts of H₂ produced under photo-assisted thermocatalytic condition and in the purely thermocatalytic condition, respectively.

2.3. Catalyst characterizations

The contents of Cu and Co in catalysts were analyzed by an inductively coupled plasma optical emission spectrometer (ICP-OES, Agilent 5110). The ultraviolet–visible absorption spectra were obtained using a UV–vis spectrophotometer (UV-2600, Shimadzu). X-ray diffraction (XRD) patterns and surface electronic states were acquired by an X-ray powder diffractometer with Cu K α radiation (PANalytical) and X-ray photoelectron spectroscopy (XPS, Escalab 250 Xi, Thermo Scientific), respectively. Transmission electron microscopy (TEM) and high-resolution TEM images were conducted on a spherical aberration (Cs-corrected) TEM (JEOL JEM ARM-200 F). Diffuse reflectance infrared Fourier transform spectroscopy (DRIFTS) analysis was operated on a FT-IR 6300 system (JASCO Corp.), which is equipped with an in-situ cell and a liquid nitrogen-cooled mercury-cadmium-telluride (MCT) detector.

Details for in-situ DRIFTS measurement and theoretical calculations are available in the [supplementary material](#).

3. Results and discussion

3.1. Catalyst characterization

Pristine Cu and a series of highly dilute CoCu plasmonic alloy NPs, with atomic ratios of Co (Table S1) ranging from 0.04% to 0.15% (named as $\text{Co}_{0.04}\text{Cu}_{99.96}$, $\text{Co}_{0.08}\text{Cu}_{99.92}$, and $\text{Co}_{0.15}\text{Cu}_{99.85}$, respectively), were deposited on inert SiO_2 supporter through wet chemistry method. TEM and STEM images show that $\text{Co}_{0.08}\text{Cu}_{99.92}$ NPs were supported by SiO_2 with an average diameter of 3 nm (Fig. 1a and Fig. S1). Lattice

fringe of 0.21 nm assigned to (111) plane of Cu indicates that introducing a trace amount of Co did not change the lattice spacing enormously (Fig. 1b). No aggregation of Co species verifies the formation of a random CoCu alloy, which is further supported by a nearly homogeneous distribution of Co on a single $\text{Co}_{0.08}\text{Cu}_{99.92}$ nanoparticle from STEM energy dispersive X-ray spectrometry (STEM-EDS) mapping (Fig. 1c-f). The X-ray diffraction (XRD) patterns (Fig. 1g) further reveal that Cu and CoCu alloy all displayed similar diffraction peaks of metallic Cu. The appearance of weak diffraction peak at around 36.6° might attribute to Cu_2O , which could be generated from the oxidation of Cu

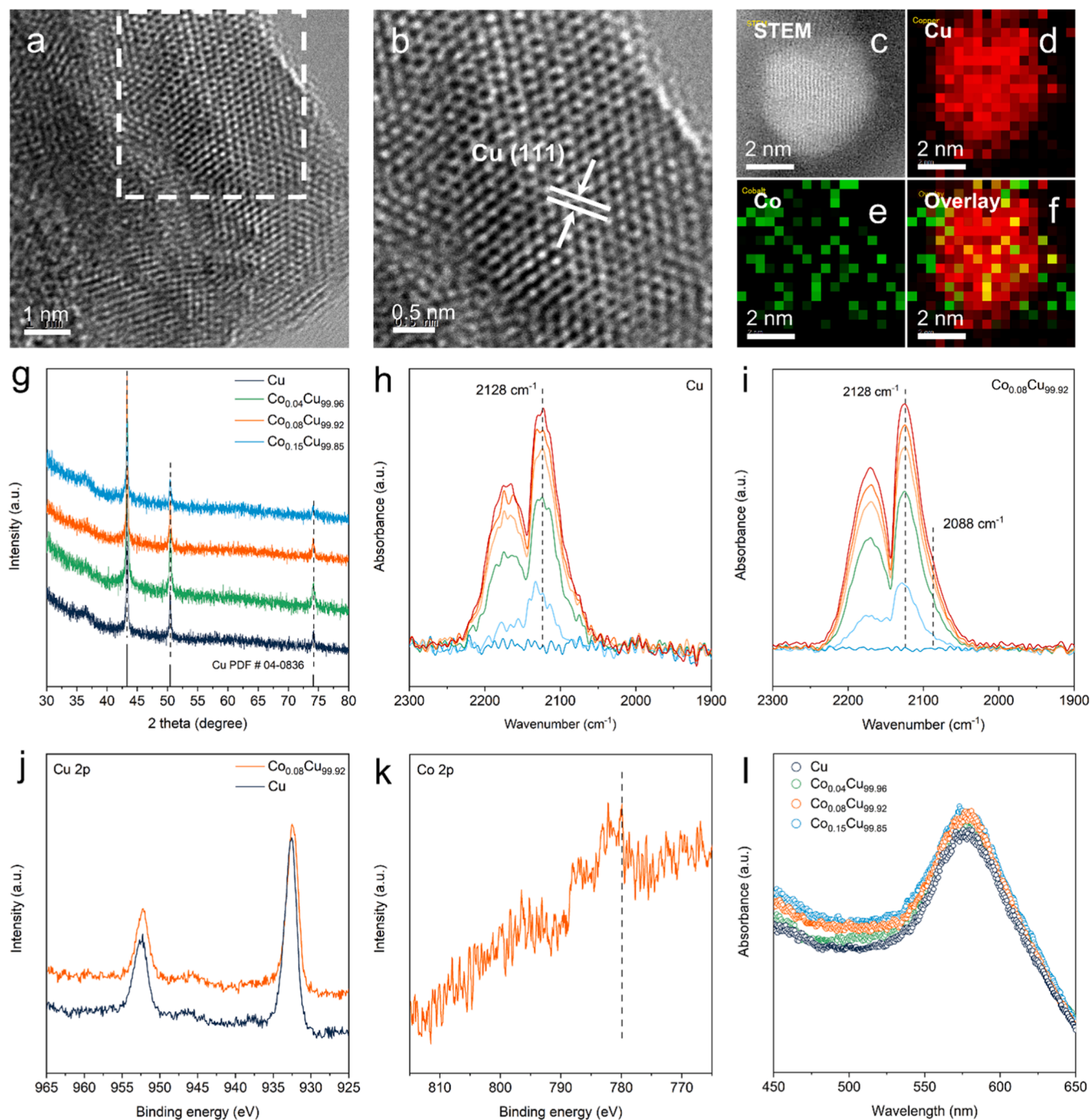


Fig. 1. Structural and chemical properties of Cu and CoCu plasmonic alloy catalysts. (a) TEM image of $\text{Co}_{0.08}\text{Cu}_{99.92}$. (b) HR-TEM image of $\text{Co}_{0.08}\text{Cu}_{99.92}$. (c-f) STEM-EDS mapping of $\text{Co}_{0.08}\text{Cu}_{99.92}$. (g) XRD patterns of Cu and CoCu catalysts. The catalysts were treated using sacrificial support method, followed by H_2 reduction. (h and i) CO-DRIFTS spectra of pristine Cu and $\text{Co}_{0.08}\text{Cu}_{99.92}$, respectively. (j) XPS Cu 2p spectra of Cu and $\text{Co}_{0.08}\text{Cu}_{99.92}$. (k) XPS Co 2p spectrum of $\text{Co}_{0.08}\text{Cu}_{99.92}$ catalyst. (l) UV-vis absorption spectra of Cu and CoCu catalysts.

due to the long-term exposure to air during XRD measurement. No peak corresponding to Co was observed, which could be attributed to high dispersion and low concentration of Co in Cu.

Surface structures of Cu and $\text{Co}_{0.08}\text{Cu}_{99.92}$ NPs were analyzed by in-situ diffuse reflectance infrared spectroscopy using CO as probe molecules (in-situ CO DRIFTS). Upon CO adsorption on Cu, two peaks appeared at 2170 and 2128 cm^{-1} , which could be assigned to the R branches of gaseous CO and atop binding of CO on Cu NPs, respectively (Fig. 1h) [42]. Compared to pristine Cu, the CO DRIFTS spectra of $\text{Co}_{0.08}\text{Cu}_{99.92}$ sample display an additional shoulder peak at 2088 cm^{-1} , indicating linearly coordinated CO to metallic Co centers on the surface of the Cu catalysts (Fig. 1i) [43]. The high-resolution Cu 2p X-ray photoelectron spectroscopy (XPS) spectrum of pristine Cu displays the binding energy of Cu 2p_{3/2} peak at 932.5 eV without noticeable satellite peaks, indicating the formation of metallic Cu (Fig. 1j) [44]. Compared to Cu, the Cu 2p_{3/2} peak of $\text{Co}_{0.08}\text{Cu}_{99.92}$ slightly shifts towards a lower value (0.1 eV, located at 932.4 eV), which might relate to electronic interaction between Cu and Co species. The Cu XPS Auger peaks of Cu and $\text{Co}_{0.08}\text{Cu}_{99.92}$ (918.7 eV) further confirm the metallic state of Cu in both samples (Fig. S2). The peak of Co 2p_{3/2} locating at 780.0 eV could be attributed to metallic Co (Fig. 1k) [45]. Above structural and chemical characterization results concertedly suggest the existence of Co atoms on the surface of Cu, forming CoCu alloy. Strong localized surface plasmon resonance (LSPR) absorption peaks (approximately 570 nm) can be observed in both pristine Cu and CoCu alloy samples, suggesting that adding small amounts of Co on Cu did not affect the optical property significantly (Fig. 1l).

3.2. Solar-driven MSR over CoCu plasmonic catalysts

Solar-driven catalytic MSR was carried out on a solar-driven reactor (Fig. S3) to manifest the catalytic behaviors of plasmonic Cu and CoCu alloy catalysts. A concentrated solar light simulated by AM 1.5 G illuminant was used as the irradiance. As shown in Fig. 2a, the temperature and light intensity of pure Cu and CoCu alloy catalysts all display positive correlations under light irradiation. The highest surface temperature of 253 °C was detected at a maximum light intensity. Nevertheless, unlike surface temperature, the Cu and CoCu alloy catalysts deliver substantially distinct catalytic behaviors under identical light irradiation condition (Fig. 2b). All CoCu alloy catalysts exhibit higher catalytic performances compared to pure Cu, especially for the alloy catalyst $\text{Co}_{0.08}\text{Cu}_{99.92}$, which displays the highest H_2 generation rate of 6225.1 $\mu\text{mol g}^{-1} \text{min}^{-1}$ (31.1 $\mu\text{mol min}^{-1}$ using 5 mg of catalysts). The production rates of H_2 display a positive relationship with catalyst amounts (Fig. S4). The addition of excessive Co in Cu did not further facilitate the reaction, which might suggest a cooperative contribution of Co/Cu dual active sites in the optimized catalysts (Fig. 2b).

Compared to conventional photocatalytic or thermocatalytic processes under even higher reaction temperatures, $\text{Co}_{0.08}\text{Cu}_{99.92}$ demonstrated an outstanding catalytic performance (Table S2). The solar-to-energy conversion efficiencies exhibit a progressive enhancement with the increasing light intensities, reaching a maximum value of 1.4% for $\text{Co}_{0.08}\text{Cu}_{99.92}$, which is approximately three times of that pristine Cu (Fig. 2c). Furthermore, the catalytic performance of $\text{Co}_{0.08}\text{Cu}_{99.92}$ alloy catalyst presents an order of magnitude higher than that of noble-metal-based materials, which are typically regarded as representative materials for MSR (Fig. 2d). Only a trace amount of undesirable CO was

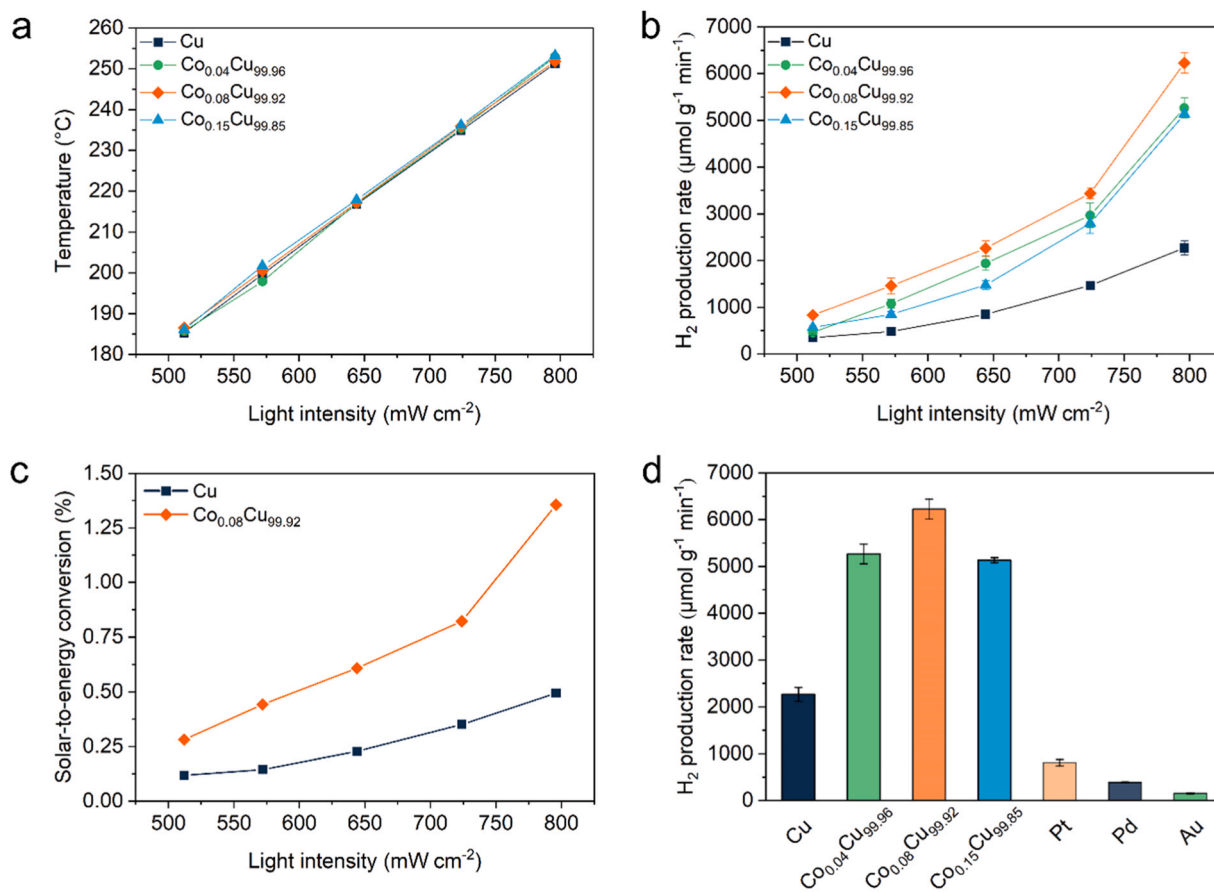


Fig. 2. Catalytic behaviors for light-driven MSR. (a) Surface temperatures of Cu and CoCu alloy catalysts upon light irradiation. (b) Catalytic performances for solar-driven MSR of Cu and CoCu plasmonic catalysts. (c) Solar-to-energy conversion efficiencies of Cu and $\text{Co}_{0.08}\text{Cu}_{99.92}$. (d) Catalytic performances of pristine Cu, CoCu alloy, and noble-metal-based catalysts.

observed on $\text{Co}_{0.08}\text{Cu}_{99.92}$ plasmonic alloy without noticeable production of other organic products (e.g., CH_2O and HCOOH), whereas the Pd/SiO_2 displayed higher selectivity of 53.8% towards CO (Table S3). In addition, $\text{Co}_{0.08}\text{Cu}_{99.92}$ plasmonic alloy catalysts manifest a stable catalytic performance under solar-driven condition without obvious deactivation for 30-hour operation (Fig. S5). The nearly unchanged structures and valence states of catalysts confirm the high stability of the $\text{Co}_{0.08}\text{Cu}_{99.92}$ alloy catalysts (Fig. S6–8).

3.3. Contribution of hot carriers during MSR

To probe the contribution of hot-carriers during reaction, photo-assisted thermocatalytic MSR was executed (Fig. S9). In order to alleviate the influence of photothermal heating, only visible light ($420 < \lambda < 720 \text{ nm}$, 423.6 mW cm^{-2}) was irradiated on the catalysts (Fig. S10). Under dark condition, reaction rate of pure Cu increases with the rising reaction temperature, reaching a maximum value of $460.1 \mu\text{mol g}^{-1} \text{ min}^{-1}$ at 220°C (Fig. 3a). Adding a small amount of Co can promote the reaction effectively (Fig. 3a), and a H_2 generation rate of $715.9 \mu\text{mol g}^{-1} \text{ min}^{-1}$ is observed at 220°C , indicating that Co could serve as an additional active site to activate CH_3OH or H_2O towards MSR. Under visible light irradiation, the catalytic performances of both Cu and $\text{Co}_{0.08}\text{Cu}_{99.92}$ plasmonic alloys are enormously enhanced, with a much higher yield of H_2 ($2532.9 \mu\text{mol g}^{-1} \text{ min}^{-1}$) for $\text{Co}_{0.08}\text{Cu}_{99.92}$ (Fig. 3a). The rate enhancement under light irradiation demonstrates its superiority at lower temperatures, as evidenced by the decline in the enhancement of reaction rate for $\text{Co}_{0.08}\text{Cu}_{99.92}$ from 5.1 to 3.5 times as the temperature rose from 180°C to 220°C (Fig. S11), whereas the disparity in H_2 production rates increases with the rise in temperature (Fig. S12). We propose that the observed visible-light-enhanced activity might be

attributed to the hot carriers from plasmonic Cu, and this assumption is further verified by the linear dependence between reaction rates and light intensities (Fig. 3b and Fig. S13 for the output irradiance of visible light in different intensities) [46].

To unravel the intrinsic reaction mechanism of both Co active sites and photo-induced charge carriers, the reaction kinetics of MSR under different reaction conditions were investigated. Through fitting of the reaction rates using the Arrhenius plot ($\ln r = -E_a/RT + \ln A$), we calculated the apparent activation energy (E_a) (Fig. 3c). The E_a of pristine Cu in the absence of light is $100.8 \text{ kJ mol}^{-1}$, and decreases to 86.6 kJ mol^{-1} after introduction of Co, verifying that Co active sites could facilitate the rate determining step of MSR (Fig. 3c). Adding visible light leads to an enormous decrease of E_a (68.2 kJ mol^{-1}), further illustrating a distinctive role of visible-light-induced hot carriers beyond simple photothermal heating (Fig. 3c). To further verify the contribution of photo-induced hot-carriers from plasmonic Cu, additional E_a was calculated under the irradiation in different wavelength region ($380 < \lambda < 520$, and $580 < \lambda < 720$, respectively) (Fig. S14). The results show that the E_a ($380 < \lambda < 520$, $E_a = 76.7 \text{ kJ mol}^{-1}$; and $580 < \lambda < 720$, $E_a = 77.7 \text{ kJ mol}^{-1}$) are evidently higher than that under the visible light irradiation ($420 < \lambda < 720 \text{ nm}$, $E_a = 68.2 \text{ kJ mol}^{-1}$), suggesting the pivotal role of photo-induced charge carriers from Cu LSPR absorption (Fig. S15). The contribution of hot carriers during reaction is further supported by the irradiation of monochromatic light (Fig. S16) at 220°C . As shown in Fig. 3d, the tendency of the apparent quantum efficiency (AQE) matches well with the light absorption spectra of $\text{Co}_{0.08}\text{Cu}_{99.92}$ plasmonic alloy, indicating the enhanced catalytic performance under visible light irradiation can be attributed to the excitation of LSPR [47]. In addition, no obvious loss in catalytic performance under both dark and light condition was observed after 5 h reaction

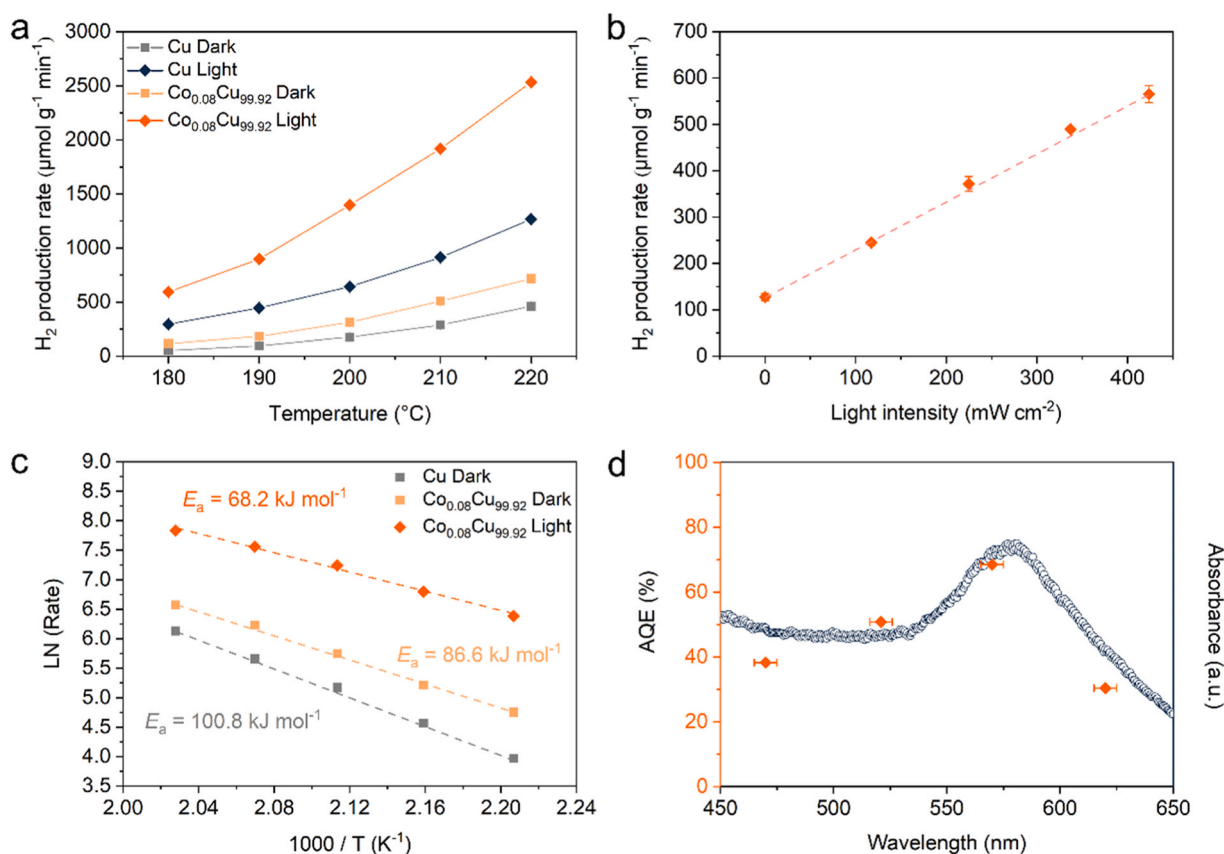


Fig. 3. Contribution of hot carriers during photo-assisted MSR. (a) Catalytic behaviors of Cu and $\text{Co}_{0.08}\text{Cu}_{99.92}$ under the dark and light conditions at different temperatures. (b) Dependence of H_2 generation rates of $\text{Co}_{0.08}\text{Cu}_{99.92}$ on light intensities at 180°C . (c) Arrhenius plots for reaction rates under different conditions. (d) Light absorption spectrum of $\text{Co}_{0.08}\text{Cu}_{99.92}$ and corresponding AQE values measured at 220°C with monochromatic light irradiation.

(Fig. S17).

3.4. Reaction mechanism of MSR over CoCu plasmonic alloy

To provide a deeper insight into the LSPR effect of plasmonic Cu and $\text{Co}_{0.08}\text{Cu}_{99.92}$, finite-difference-time-domain (FDTD) simulations were conducted. As demonstrated in Fig. 4a, under the irradiation of visible light, spatially non-homogeneous distribution of local electric field emerges around the Cu NPs, and these electric field is further intensified in the interstitial position between each plasmonic NPs, forming “hot spots” that could yield higher rates of energetic charge-carrier formation [48]. As the wavelength of monochromatic light increased from 470 to 670 nm, the electric field enhancement firstly maximizes at 570 nm,

followed by a decrease in the higher wavelength region. This tendency matches well with light absorption spectrum and corresponding AQE values (Fig. 3d), indicating that the light excitation at 570 nm might play a significant role in facilitating the reactant conversion. The addition of a small amount of Co did not modify the tendency of electric field enhancement on Cu enormously (Fig. 4a). We propose that hot carriers are generated through the decay of LSPR of Cu, and these charge carriers have the potential to participate in the surface reaction through the surface dispersed Co active sites.

The influence of hot carriers on the MSR intermediates was studied using in-situ DRIFTS measurements on $\text{Co}_{0.08}\text{Cu}_{99.92}$ under purely thermocatalytic condition or with visible light irradiation at 200 °C (Fig. 4b). Characteristic rotational vibrations of gaseous CO_2 can be

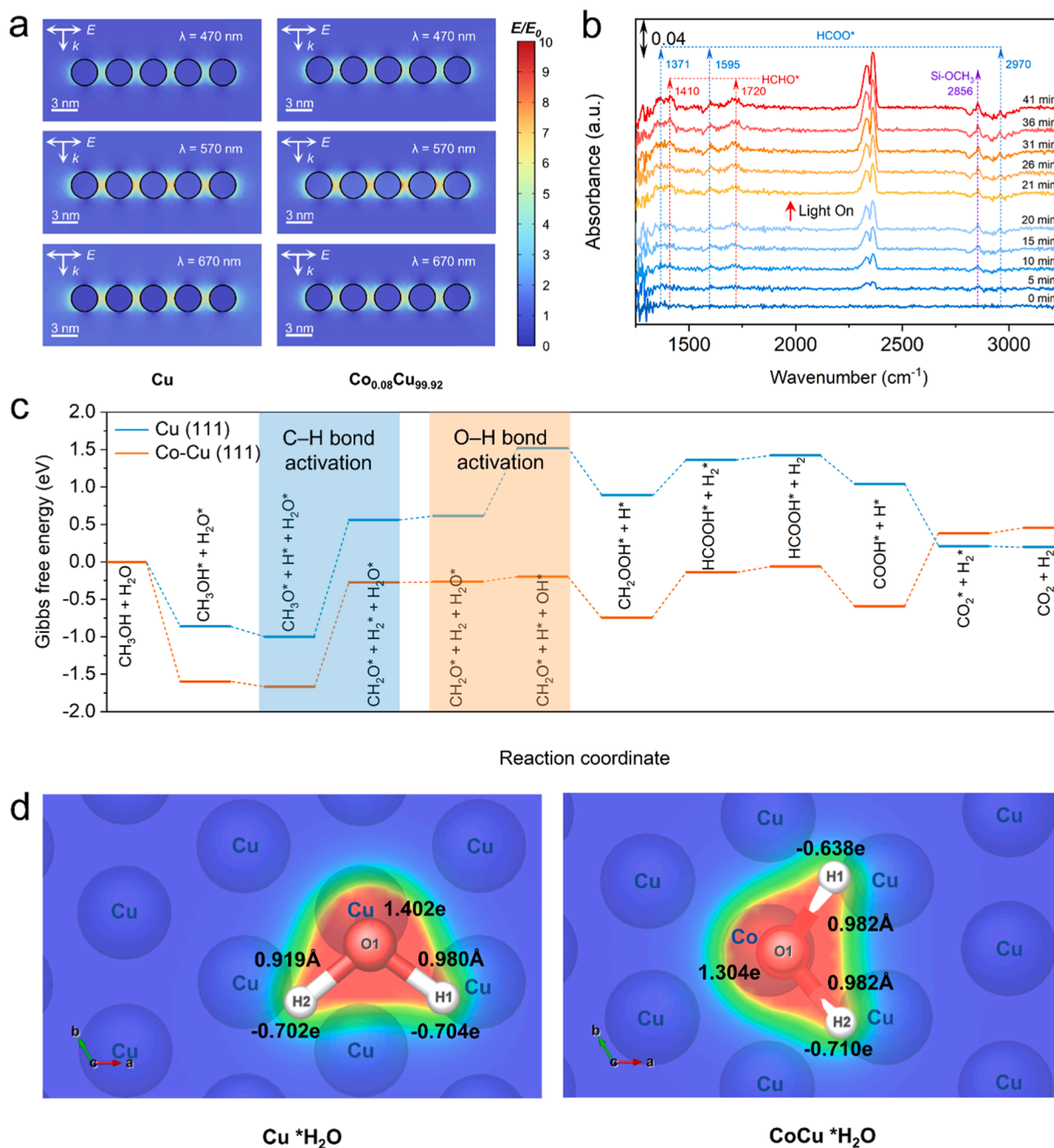


Fig. 4. Mechanistic investigations of reaction role for hot carriers and Co–Cu dual active sites. (a) Electrical field enhancement of Cu and $\text{Co}_{0.08}\text{Cu}_{99.92}$ under the irradiation with different wavelengths. (b) In-situ DRIFTS spectra of $\text{Co}_{0.08}\text{Cu}_{99.92}$ under dark and light conditions at 200 °C. (c) Calculated Gibbs free energy diagram for MSR over Cu (111) and Co-atoms-substituted Cu (111) surfaces. (d) Bader charge analysis of optimized structure during H_2O adsorption on surface of Cu and Co-atoms-substituted Cu surface, respectively. H_2O molecule is adsorbed on Co atom of CoCu surface.

observed at around 2360 cm^{-1} [32]. The C–H vibrations of Si–OCH₃ species appear at 2856 cm^{-1} [49]. As the reaction proceeded, two sets of peaks gradually emerge, which can be assigned to HCOO* (2970 , 1595 , and 1371 cm^{-1}) [50] and HCHO* (1720 and 1410 cm^{-1}) [32], respectively. The existences of these intermediates indicate that the MSR mainly proceeded through formate pathway. Upon light irradiation, the peak increment of CO₂ (2360 cm^{-1}) became more evident (Fig. 4b), in accordance with the observed rate enhancement under light condition. The absence of external absorption peaks following light exposure indicates that the photo-induced charge carriers mainly serve to accelerate the conversion of surfactants.

On the basis of the aforementioned in-situ spectroscopic investigations, density functional theory (DFT) calculations were subjected to construct a comprehensive Gibbs free energy diagram. Two surface models, namely Cu (111) and Co–Cu (111) surfaces, were firstly constructed, and their energy barriers of each elementary step for MSR are depicted in Fig. 4c. Building upon the references over Cu-based catalysts [51], the sequential steps of the MSR can be elucidated as follows: initially, the adsorbed CH₃OH species undergo dissociation, forming CH₃O* species, which are subsequently dehydrogenated into CH₂O* via C–H bond activation. The CH₂O* species interacting with OH* which is generated from H₂O dissociation produce CH₂OOH*. Further dehydrogenation of CH₂OOH* leads to the formation of HCOOH*, which could finally decompose into CO₂ and H₂. Notably, on the CoCu surface, the dissociative adsorption of CH₃OH is highly exothermic, indicating the introduction of Co active sites favors the CH₃OH adsorption and subsequent dissociation (Fig. 4c). The strong

endothermic nature in the processes of CH₃O* → CH₂O* + H* (C–H bond activation) and H₂O* → OH* + H* (H₂O dissociation) suggests the critical role in activating both CH₃OH and H₂O molecules for improving the catalytic performance. Interestingly, adding Co active sites slightly reduces the C–H bond activation energy of Cu (1.39 vs 1.56 eV), indicating that the C–H bond activation of CH₃O* species might be favorable with the assistance of surface Co, whilst such a process is dominantly controlled by Cu active sites. Furthermore, it is worthy of note that, for the water dissociation, the reaction energy for activating O–H bond on pristine Cu (0.91 eV) is much higher than that of CoCu surface (0.07 eV), revealing a decisive role of Co active site in activating H₂O molecules.

Above DFT calculations suggest that the activation of both CH₃OH and H₂O molecules are of pivotal importance for MSR with positively high Gibbs free energies, and the surface Co active sites greatly facilitate dissociative adsorption of CH₃OH and the H₂O activation. In order to disclose the reason for the reduced energy barrier of the key elementary step of H₂O dissociation over Cu–Co dual active sites, charge density difference was simulated using Bader charge analysis. Fig. 4d compares the charge density difference as well as bond length of O–H in H₂O* adsorbed on pristine Cu and CoCu substrate, respectively. Theoretically, the prolonged bond length weakens the corresponding bond strength, leading to bond activation [52]. Indeed, in comparison to H₂O* on Cu (average O–H bond length of 0.950 Å), the O–H bonds are greatly elongated on CoCu surface with an average bond length of 0.982 Å , suggesting that the interactions between H₂O* and surface Co sites facilitate the activation of O–H bond for water dissociation. From the perspective of atomic charges, the adsorption of H₂O on CoCu

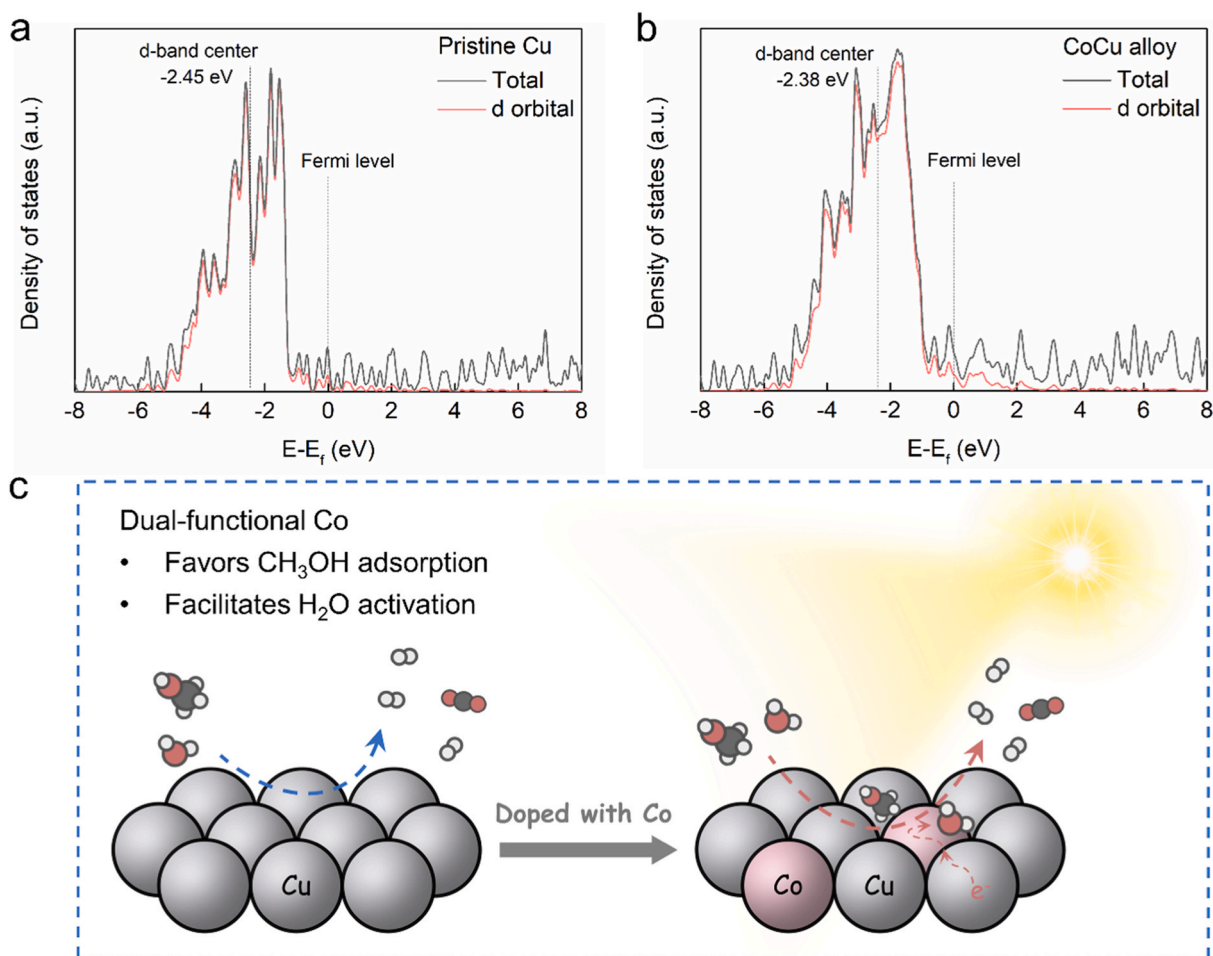


Fig. 5. Density of states (DOS) calculations and schematic illustration of reaction mechanism. (a) DOS of pristine Cu. (b) DOS of CoCu alloy. (c) Schematic illustration of reaction mechanism for light-driven methanol steam reforming over Cu and CoCu plasmonic alloy catalysts.

surface significantly redistributes the charges of H₂O, and the substantial difference of atomic charges in H1 and H2 could lead to the local polarization, thereby facilitating the dissociation of H₂O molecules.

Moreover, the electronic structures of the pristine Cu and CoCu alloy were investigated using density of states (DOS) calculation in order to unravel how Co active site could promote the CH₃OH adsorption (Fig. 5a and b). The electronic structure results suggest the metallic nature of both Cu and CoCu alloy catalysts, and more interestingly, the d-band center of CoCu alloy (−2.38 eV) is closer to the Fermi level than that of pristine Cu (−2.45 eV). The upward shift of the d-band center results in an elevated anti-bonding state, which can increase the interaction between surface atoms (Co) and adsorbates (CH₃OH) [53]. Based on the above evidences, we can establish a compelling argument for the vital role of Co active sites in the dissociative adsorption of CH₃OH molecules and the reduction of energy barrier in the rate-determining step of H₂O dissociation. The distinctive capability of Co active sites working in conjunction with Cu leads to an amplified catalytic performance.

Our mechanistic investigations sculpture a comprehensive picture of Co–Cu bimetallic active site, elucidating how it functions as an efficient catalyst for MSR under light irradiation (Fig. 5c). Plasmonic Cu NPs absorb visible light irradiation to produce hot carriers, and these energetic electrons may transfer to surface Co active sites, leaving electron-deficient Cu. The negatively charged Co could facilitate the H₂O reduction, whereas the positively charged Cu is considered to be responsible for CH₃OH oxidation. On the other hand, due to the superior capacity of Co active sites in adsorbing CH₃OH, a smooth production of *CH₂O species through C–H bond activation may be occurred at the interface between Cu and Co. These produced *CH₂O intermediates could be subsequently converted through the interaction with *OH (product of H₂O activation), rendering a more rapid surface catalytic transformation. The cooperative bond activation processes, together with charge transfer and photothermal heating, concertedly contribute to an outstanding performance of solar-driven photocatalysis over CoCu alloy catalysts (Fig. 5c).

4. Conclusion

In conclusion, CoCu bimetallic alloy catalysts with a high dispersion of Co active sites on plasmonic Cu were successfully synthesized. The CoCu catalyst exhibited an outstanding activity for solar-driven methanol steam reforming, delivering a H₂ production rate of 6225.1 μmol g^{−1} min^{−1}. Detailed experimental and theoretical investigations, including in-situ DRIFTS studies and various DFT simulations, suggested that surface Co active sites favored the CH₃OH adsorption and H₂O activation simultaneously. Hot electrons produced by LSPR of Cu could further promote the CH₃OH/H₂O activation on dual Co–Cu active sites, thereby enhancing the kinetics of H₂ production at Co–Cu interface. Our study unveils a novel and highly effective method for harnessing renewable solar energy to produce H₂ from CH₃OH and H₂O, thus expanding the horizons of research focused on developing alloy materials for sustainable H₂ production from various biomass-derived hydrogen carriers.

CRedit authorship contribution statement

Wen-Ning Lu: Investigation, Formal analysis, Validation, Writing – original draft, Writing – review & editing, Funding acquisition. **Shunqin Luo:** Conceptualization, Formal analysis, Writing – review & editing. **Yibo Zhao:** Formal analysis. **Jianbing Xu:** Formal analysis. **Gaoliang Yang:** Formal analysis. **Emmanuel Picheau:** Formal analysis, Writing – review & editing. **Minmin Han:** Formal analysis. **Qi Wang:** Methodology, Software, Writing – original draft. **Sijie Li:** Formal analysis. **Lulu Jia:** Formal analysis. **Ming-Xing Ling:** Supervision, Writing – review & editing. **Tetsuya Kako:** Resources. **Jinhua Ye:** Project administration, Supervision, Resources, Funding acquisition, Writing – review & editing.

Declaration of Competing Interest

The authors declare that they have no known competing financial interests or personal relationships that could have appeared to influence the work reported in this paper.

Data Availability

Data will be made available on request.

Acknowledgements

This work was funded by the National Natural Science Foundation of China (42103016), State Key Laboratory of Nuclear Resources and Environment (2020Z20), JSPS KAKENHI (JP18H02065), the World Premier International Research Center Initiative (WPI Initiative) on Materials Nanoarchitectonics (MANA), MEXT (Japan), and Photoexcitonix Project in Hokkaido University. A part of DFT calculations in this study were performed on the Numerical Materials Simulator at NIMS. TEM characterization was supported by NIMS Electron Microscopy Analysis Station, Nanostructural Characterization Group.

Appendix A. Supporting information

Supplementary data associated with this article can be found in the online version at doi:10.1016/j.apcatb.2023.123520.

References

- [1] H. Lin, S. Luo, H. Zhang, J. Ye, Toward solar-driven carbon recycling, *Joule* 6 (2022) 294–314, <https://doi.org/10.1016/j.joule.2022.01.001>.
- [2] X. Yang, C.P. Nielsen, S. Song, M.B. McElroy, Breaking the hard-to-abate bottleneck in China's path to carbon neutrality with clean hydrogen, *Nat. Energy* 7 (2022) 955–965, <https://doi.org/10.1038/s41560-022-01114-6>.
- [3] Z. Liu, Z. Deng, G. He, H. Wang, X. Zhang, J. Lin, Y. Qi, X. Liang, Challenges and opportunities for carbon neutrality in China, *Nat. Rev. Earth Environ.* 3 (2022) 141–155, <https://doi.org/10.1038/s43017-021-00244-x>.
- [4] Y. Yuan, L. Zhou, H. Robotjazi, J.L. Bao, J. Zhou, A. Bayles, L. Yuan, M. Lou, M. Lou, S. Khatiwada, E.A. Carter, P. Nordlander, N.J. Halas, Earth-abundant photocatalyst for H₂ generation from NH₃ with light-emitting diode illumination, *Science* 378 (2022) 889–893, <https://doi.org/10.1126/science.abn5636>.
- [5] M.Z. Jacobson, W. Colella, D. Golden, Cleaning the air and improving health with hydrogen fuel-cell vehicles, *Science* 308 (2005) 1901–1905, <https://doi.org/10.1126/science.1109157>.
- [6] R.L. Cohen, J. Wernick, Hydrogen storage materials: properties and possibilities, *Science* 214 (1981) 1081–1087, <https://doi.org/10.1126/science.214.4525.1081>.
- [7] H. Song, S. Luo, H. Huang, B. Deng, J. Ye, Solar-driven hydrogen production: recent advances, challenges, and future perspectives, *ACS Energy Lett.* 7 (2022) 1043–1065, <https://doi.org/10.1021/acsenenergylett.1c02591>.
- [8] J. Oh, Y. Jo, T.W. Kim, H.B. Bathula, S. Yang, J.H. Baik, Y.-W. Suh, Highly efficient and robust Pt ensembles on mesoporous alumina for reversible H₂ charge and release of commercial benzyltoluene molecules, *Appl. Catal. B Environ.* 305 (2022), 121061, <https://doi.org/10.1016/j.apcatb.2022.121061>.
- [9] C. Martin, A. Quintanilla, G. Vega, J.A. Casas, Formic acid-to-hydrogen on Pd/AC catalysts: kinetic study with catalytic deactivation, *Appl. Catal. B Environ.* 317 (2022), 121802, <https://doi.org/10.1016/j.apcatb.2022.121802>.
- [10] L. Lin, Q. Yu, M. Peng, A. Li, S. Yao, S. Tian, X. Liu, A. Li, Z. Jiang, R. Gao, X. Han, Y.-w Li, X.-d Wen, W. Zhou, D. Ma, Atomically dispersed Ni/α-MoC catalyst for hydrogen production from methanol/water, *J. Am. Chem. Soc.* 143 (2021) 309–317, <https://doi.org/10.1021/jacs.0c10776>.
- [11] L. Chen, Z. Qi, X. Peng, J.-L. Chen, C.-W. Pao, X. Zhang, C. Dun, M. Young, D. Prendergast, J.J. Urban, J. Guo, G.A. Somorjai, J. Su, Insights into the mechanism of methanol steam reforming tandem reaction over CeO₂ supported single-site catalysts, *J. Am. Chem. Soc.* 143 (2021) 12074–12081, <https://doi.org/10.1021/jacs.1c03895>.
- [12] Y.-J. Liu, H.-F. Kang, X.-N. Hou, S.-J. Qing, L. Zhang, Z.-X. Gao, H.-W. Xiang, Sustained release catalysis: dynamic copper releasing from stoichiometric spinel CuAl₂O₄ during methanol steam reforming, *Appl. Catal. B Environ.* 323 (2023), 122043, <https://doi.org/10.1016/j.apcatb.2022.122043>.
- [13] D.R. Palo, R.A. Dagle, J.D. Holladay, Methanol steam reforming for hydrogen production, *Chem. Rev.* 107 (2007) 3992–4021, <https://doi.org/10.1021/cr050198b>.
- [14] S. Sá, H. Silva, L. Brandão, J.M. Sousa, A. Mendes, Catalysts for methanol steam reforming—a review, *Appl. Catal. B Environ.* 99 (2010) 43–57, <https://doi.org/10.1016/j.apcatb.2010.06.015>.
- [15] L. Lin, W. Zhou, R. Gao, S. Yao, X. Zhang, W. Xu, S. Zheng, Z. Jiang, Q. Yu, Y.-W. Li, C. Shi, X.-D. Wen, D. Ma, Low-temperature hydrogen production from water and

- methanol using Pt/ α -MoC catalysts, *Nature* 544 (2017) 80–83, <https://doi.org/10.1038/nature21672>.
- [16] Y. Wang, B. Liu, Q. Guo, Y. Sun, S. Zhang, Y. Qu, Stabilized *OH species by K^+ -doped Pt for H_2 generation with ultra-low levels of CO through aqueous-phase reforming of methanol at low temperature, *Appl. Catal. B Environ.* 338 (2023), 123011, <https://doi.org/10.1016/j.apcatb.2023.123011>.
- [17] J. Zhang, X. Tan, L. Shi, H. Chen, Y. Liu, S. Wang, X. Duan, M. Wu, H. Sun, S. Wang, Tandem internal electric fields in intralayer/interlayer carbon nitride homojunction with a directed flow of photo-excited electrons for photocatalysis, *Appl. Catal. B Environ.* 333 (2023), 122781, <https://doi.org/10.1016/j.apcatb.2023.122781>.
- [18] Y. Yang, Z. Chen, H. Huang, Y. Liu, J. Zou, S. Shen, J. Yan, J. Zhang, Z. Zhuang, Z. Luo, C. Yang, Y. Yu, Z. Zou, Synergistic surface activation during photocatalysis on perovskite derivative sites in heterojunction, *Appl. Catal. B Environ.* 323 (2023), 122146, <https://doi.org/10.1016/j.apcatb.2022.122146>.
- [19] C. Lv, X. Bai, S. Ning, C. Song, Q. Guan, B. Liu, Y. Li, J. Ye, Nanostructured materials for photothermal carbon dioxide hydrogenation: regulating solar utilization and catalytic performance, *ACS Nano* 17 (2023) 1725–1738, <https://doi.org/10.1021/acsnano.2c09025>.
- [20] L. Zhou, J.M.P. Martinez, J. Finzel, C. Zhang, D.F. Swearer, S. Tian, H. Robatjazi, M. Lou, L. Dong, L. Henderson, P. Christopher, E.A. Carter, P. Nordlander, N. J. Halas, Light-driven methane dry reforming with single atomic site antenna-reactor plasmonic photocatalysts, *Nat. Energy* 5 (2020) 61–70, <https://doi.org/10.1038/s41560-019-0517-9>.
- [21] L. Zhou, D.F. Swearer, C. Zhang, H. Robatjazi, H. Zhao, L. Henderson, L. Dong, P. Christopher, E.A. Carter, P. Nordlander, N.J. Halas, Quantifying hot carrier and thermal contributions in plasmonic photocatalysis, *Science* 362 (2018) 69–72, <https://doi.org/10.1126/science.aat6967>.
- [22] H. Tada, Rational design for gold nanoparticle-based plasmonic catalysts and electrodes for water oxidation towards artificial photosynthesis, *Dalton Trans.* 51 (2022) 3383–3393, <https://doi.org/10.1039/D1DT04020K>.
- [23] R. Kojima, Y. Ogino, S.-i. Naya, T. Soejima, H. Tada, Seed-assisted hydrothermal synthesis of radial TiO_2 homomocrystals and the application as a support for plasmonic photocatalysts, *Cryst. Growth Des.* 23 (2023) 4472–4479, <https://doi.org/10.1021/acs.cgd.3c00220>.
- [24] H. Inoue, S.-i. Naya, A. Akita, H. Sugime, H. Tada, Photothermal oxidation of cinnamyl alcohol with hydrogen peroxide catalyzed by gold nanoparticle/antimony-doped tin oxide nanocrystals, *Chem. Eur. J.* 28 (2022), e202201653, <https://doi.org/10.1002/chem.202201653>.
- [25] C. Hu, X. Chen, J. Jin, Y. Han, S. Chen, H. Ju, J. Cai, Y. Qiu, C. Gao, C. Wang, Z. Qi, R. Long, L. Song, Z. Liu, Y. Xiong, Surface plasmon enabling nitrogen fixation in pure water through a dissociative mechanism under mild conditions, *J. Am. Chem. Soc.* 141 (2019) 7807–7814, <https://doi.org/10.1021/jacs.9b01375>.
- [26] J. Yang, Y. Guo, R. Jiang, F. Qin, H. Zhang, W. Lu, J. Wang, J.C. Yu, High-efficiency “working-in-tandem” nitrogen photofixation achieved by assembling plasmonic gold nanocrystals on ultrathin titania nanosheets, *J. Am. Chem. Soc.* 140 (2018) 8497–8508, <https://doi.org/10.1021/jacs.8b03537>.
- [27] B. Deng, H. Song, Q. Wang, J. Hong, S. Song, Y. Zhang, K. Peng, H. Zhang, T. Kako, J. Ye, Highly efficient and stable photothermal catalytic CO_2 hydrogenation to methanol over Ru/In_2O_3 under atmospheric pressure, *Appl. Catal. B Environ.* 327 (2023), 122471, <https://doi.org/10.1016/j.apcatb.2023.122471>.
- [28] K. Peng, J. Ye, H. Wang, H. Song, B. Deng, S. Song, Y. Wang, L. Zuo, J. Ye, Natural halloysite nanotubes supported Ru as highly active catalyst for photothermal catalytic CO_2 reduction, *Appl. Catal. B Environ.* 324 (2023), 122262, <https://doi.org/10.1016/j.apcatb.2022.122262>.
- [29] K.M. Kamal, R. Narayan, N. Chandran, S. Popović, M.A. Nazrulla, J. Kovač, N. Vrtovec, M. Bele, N. Hodnik, M.M. Kržmanc, B. Likozar, Synergistic enhancement of photocatalytic CO_2 reduction by plasmonic Au nanoparticles on TiO_2 decorated N-graphene heterostructure catalyst for high selectivity methane production, *Appl. Catal. B Environ.* 307 (2022), 121181, <https://doi.org/10.1016/j.apcatb.2022.121181>.
- [30] S. Luo, X. Ren, H. Lin, H. Song, J. Ye, Plasmonic photothermal catalysis for solar-to-fuel conversion: current status and prospects, *Chem. Sci.* 12 (2021) 5701–5719, <https://doi.org/10.1039/D1SC00064K>.
- [31] R. Kojima, S.-i. Naya, H. Tada, Three-dimensional plasmonic photocatalyst consisting of faceted gold nanoparticles and radial titanium(IV) oxide heteromocrystals, *J. Phys. Chem. C* 127 (2023) 3478–3485, <https://doi.org/10.1021/acs.jpcc.2c08793>.
- [32] S. Luo, H. Lin, Q. Wang, X. Ren, D. Hernández-Pinilla, T. Nagao, Y. Xie, G. Yang, S. Li, H. Song, M. Oshikiri, J. Ye, Triggering water and methanol activation for solar-driven H_2 production: interplay of dual active sites over plasmonic ZnCu alloy, *J. Am. Chem. Soc.* 143 (2021) 12145–12153, <https://doi.org/10.1021/jacs.1c04315>.
- [33] S. Deng, B. Zhang, P. Choo, P.J.M. Smeets, T.W. Odom, Plasmonic photoelectrocatalysis in copper-platinum core-shell nanoparticle lattices, *Nano Lett.* 21 (2021) 1523–1529, <https://doi.org/10.1021/acs.nanolett.0c05029>.
- [34] H. Robatjazi, J.L. Bao, M. Zhang, L. Zhou, P. Christopher, E.A. Carter, P. Nordlander, N.J. Halas, Plasmon-driven carbon-fluorine ($C(sp^3)-F$) bond activation with mechanistic insights into hot-carrier-mediated pathways, *Nat. Catal.* 3 (2020) 564–573, <https://doi.org/10.1038/s41929-020-0466-5>.
- [35] X. Zhang, Y. Fan, E. You, Z. Li, Y. Dong, L. Chen, Y. Yang, Z. Xie, Q. Kuang, L. Zheng, MOF encapsulated sub-nm Pd skin/Au nanoparticles as antenna-reactor plasmonic catalyst for light driven CO_2 hydrogenation, *Nano Energy* 84 (2021), 105950, <https://doi.org/10.1016/j.nanoen.2021.105950>.
- [36] L. Zhao, J. Duan, Q. Zhang, Y. Li, K. Fang, Preparation, structural characteristics, and catalytic performance of Cu–Co alloy supported on Mn–Al oxide for higher alcohol synthesis via syngas, *Ind. Eng. Chem. Res.* 57 (2018) 14957–14966, <https://doi.org/10.1021/acs.iecr.8b03304>.
- [37] T.-y. Chen, J. Su, Z. Zhang, C. Cao, X. Wang, R. Si, X. Liu, B. Shi, J. Xu, Y.-F. Han, Structure evolution of Co–CoO_x interface for higher alcohol synthesis from syngas over Co/CeO₂ catalysts, *ACS Catal.* 8 (2018) 8606–8617, <https://doi.org/10.1021/acscatal.8b00453>.
- [38] S. Ning, H. Ou, Y. Li, C. Lv, S. Wang, D. Wang, J. Ye, Co^0-Co^{0+} interface double-site-mediated C–C coupling for the photothermal conversion of CO_2 into light olefins, *Angew. Chem. Int. Ed.* 62 (2023), e202302253, <https://doi.org/10.1002/anie.202302253>.
- [39] R. Shi, C. Tian, X. Zhu, C.-Y. Peng, B. Mei, L. He, X.-L. Du, Z. Jiang, Y. Chen, S. Dai, Achieving an exceptionally high loading of isolated cobalt single atoms on a porous carbon matrix for efficient visible-light-driven photocatalytic hydrogen production, *Chem. Sci.* 10 (2019) 2585–2591, <https://doi.org/10.1039/C8SC05540H>.
- [40] Z. Li, J. Liu, J. Zhao, R. Shi, G.I.N. Waterhouse, X.-D. Wen, T. Zhang, Photo-driven hydrogen production from methanol and water using plasmonic Cu nanoparticles derived from layered double hydroxides, *Adv. Funct. Mater.* 33 (2023), 2213672, <https://doi.org/10.1002/adfm.202213672>.
- [41] J. Zhao, Y. Bai, Z. Li, J. Liu, W. Wang, P. Wang, B. Yang, R. Shi, G.I.N. Waterhouse, X.-D. Wen, Q. Dai, T. Zhang, Plasmonic Cu nanoparticles for the low-temperature photo-driven water-gas shift reaction, *Angew. Chem. Int. Ed.* 62 (2023), e202219299, <https://doi.org/10.1002/anie.202219299>.
- [42] J. Shan, G. Giannakakis, J. Liu, S. Cao, M. Ouyang, M. Li, S. Lee, M. Flytzani-Stephanopoulos, PdCu single atom alloys for the selective oxidation of methanol to methyl formate at low temperatures, *Top. Catal.* 63 (2020) 618–627, <https://doi.org/10.1007/s11244-020-01288-x>.
- [43] N. Kumar, K. Jothimurugesan, G.G. Stanley, V. Schwartz, J.J. Spivey, In situ FT-IR study on the effect of cobalt precursors on CO adsorption behavior, *J. Phys. Chem. C* 115 (2011) 990–998, <https://doi.org/10.1021/jp104878e>.
- [44] K. Sun, X. Gao, Y. Bai, M. Tan, G. Yang, Y. Tan, Synergetic catalysis of bimetallic copper–cobalt nanosheets for direct synthesis of ethanol and higher alcohols from syngas, *Catal. Sci. Technol.* 8 (2018) 3936–3947, <https://doi.org/10.1039/C8CY01074A>.
- [45] S. Guan, Y. Guo, H. Zhang, X. Liu, Y. Fan, B. Liu, The alloy-oxide interfacial ensemble effect of a multilayer core-shell nanomotor for hydrogen generation from ammonia borane, *Sustain. Energy Fuels* 6 (2022) 1753–1761, <https://doi.org/10.1039/D1SE01994E>.
- [46] E. Cortés, R. Grzeschik, S.A. Maier, S. Schlücker, Experimental characterization techniques for plasmon-assisted chemistry, *Nat. Rev. Chem.* 6 (2022) 259–274, <https://doi.org/10.1038/s41570-022-00368-8>.
- [47] X. Meng, L. Liu, S. Ouyang, H. Xu, D. Wang, N. Zhao, J. Ye, Nanometals for solar-to-chemical energy conversion: from semiconductor-based photocatalysis to plasmon-mediated photocatalysis and photo-thermocatalysis, *Adv. Mater.* 28 (2016) 6781–6803, <https://doi.org/10.1002/adma.201600305>.
- [48] H. Robatjazi, M. Lou, B.D. Clark, C.R. Jacobson, D.F. Swearer, P. Nordlander, N. J. Halas, Site-selective nanoreactor deposition on photocatalytic Al nanocubes, *Nano Lett.* 20 (2020) 4550–4557, <https://doi.org/10.1021/acs.nanolett.0c01405>.
- [49] H. Yang, Y. Chen, X. Cui, G. Wang, Y. Cen, T. Deng, W. Yan, J. Gao, S. Zhu, U. Olsbye, J. Wang, W. Fan, A highly stable copper-based catalyst for clarifying the catalytic roles of Cu^0 and Cu^+ species in methanol dehydrogenation, *Angew. Chem. Int. Ed.* 57 (2018) 1836–1840, <https://doi.org/10.1002/anie.201710605>.
- [50] H. Zhao, R. Yu, S. Ma, K. Xu, Y. Chen, K. Jiang, Y. Fang, C. Zhu, X. Liu, Y. Tang, L. Wu, Y. Wu, Q. Jiang, P. He, Z. Liu, L. Tan, The role of Cu_1-O_3 species in single-atom Cu/ZrO₂ catalyst for CO_2 hydrogenation, *Nat. Catal.* 5 (2022) 818–831, <https://doi.org/10.1038/s41929-022-00840-0>.
- [51] N. Takezawa, N. Iwasa, Steam reforming and dehydrogenation of methanol: Difference in the catalytic functions of copper and group VIII metals, *Catal. Today* 36 (1997) 45–56, [https://doi.org/10.1016/S0920-5861\(96\)00195-2](https://doi.org/10.1016/S0920-5861(96)00195-2).
- [52] S. Wang, F. Ichihara, H. Pang, H. Chen, J. Ye, Nitrogen fixation reaction derived from nanostructured catalytic materials, *Adv. Funct. Mater.* 28 (2018), 1803309, <https://doi.org/10.1002/adfm.201803309>.
- [53] Y. Zhao, Z. Zhang, L. Liu, Y. Wang, T. Wu, W. Qin, S. Liu, B. Jia, H. Wu, D. Zhang, X. Qu, G. Qi, E.P. Giannelis, M. Qin, S. Guo, S and O co-coordinated Mo single sites in hierarchically porous tubes from sulfur–enamine copolymerization for oxygen reduction and evolution, *J. Am. Chem. Soc.* 144 (2022) 20571–20581, <https://doi.org/10.1021/jacs.2c05247>.